A study on combination of alkaline treatment and PLA/f-CNTs composite coating on corrosion, biocompatibility and antibacterial activity of Mg alloy

ABRARI, H., AHMADI, T., NEKOUIE, Vahid, TAGHIAN DEHAGHANI, M., AMIRI, M., RAZZAGHI, M. and BAKHSHESHI-RAD, H.R.

Highlights

1. Multifunctional $Mg(OH)_2$-PLA/f-CNTs coating were prepared on Mg using the dip-coating method.

2. $Mg(OH)_2$-PLA/f-CNTs coated Mg alloy results in superior corrosion resistance and cytocompatibility than uncoated Mg alloy.

3. Antibacterial performance of $Mg(OH)_2$-PLA/f-CNTs coating increases with increasing f-CNTs concentration.

4. Corrosion and antibacterial mechanism of the $Mg(OH)_2$-PLA/f-CNTs coating on Mg alloy is proposed.

Graphical Abstract

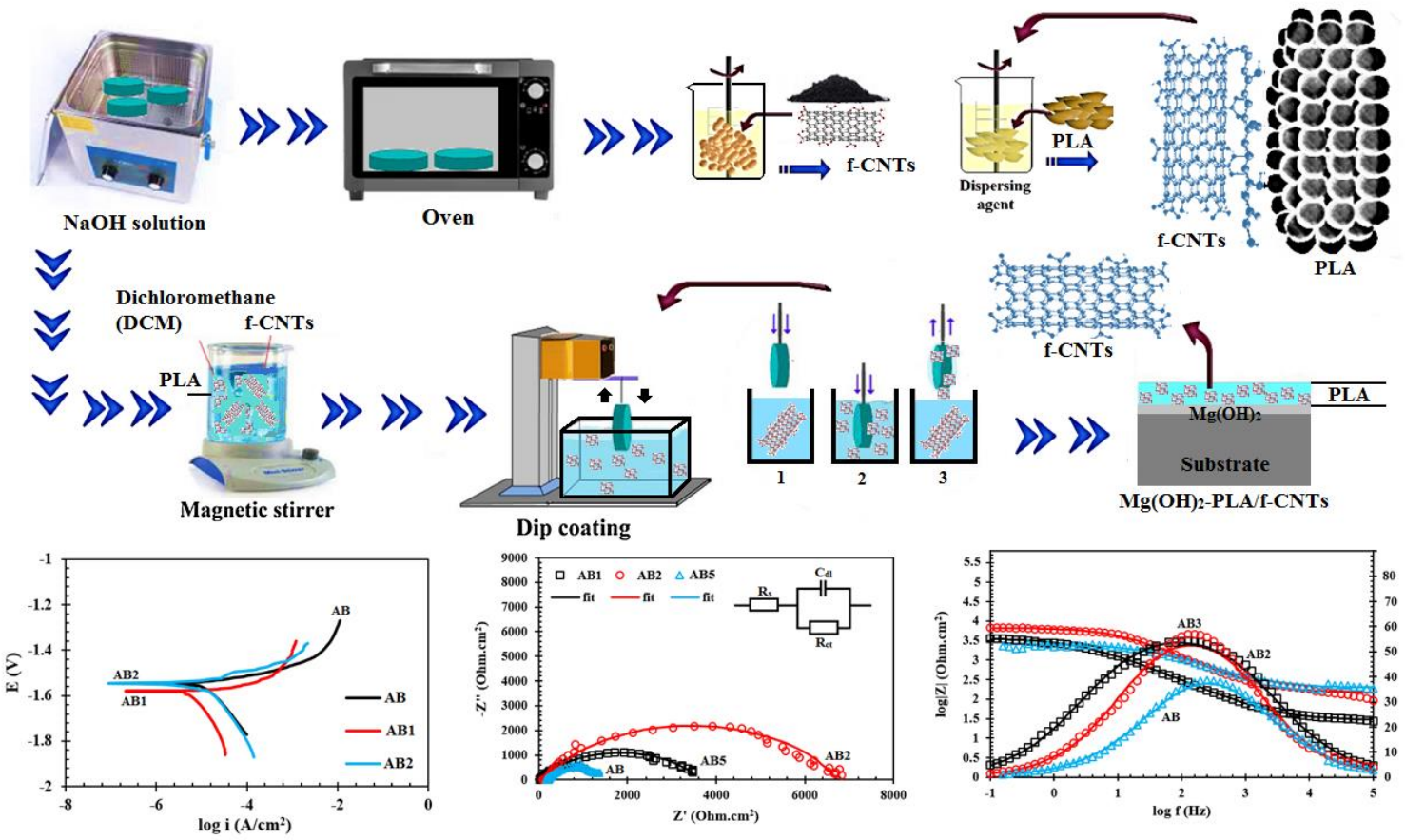

A study on combination of alkaline treatment and PLA/f-CNTs composite coating on corrosion, biocompatibility and antibacterial activity of Mg alloy

H. Abrari-Bahirlooei[a], T. Ahmadi[a,*], V. Nekouie[b,c] , M.T. Dehaghanid[d], M. Amiri[a], M. Razzaghi[e], H.R. Bakhsheshi-Rad[e,*]

[a]Department of Biomedical Engineering, Islamic Azad University, Central Tehran Branch, P.O. Box 13185/768, Tehran, Iran
[b]Department of Engineering and Mathematics, Sheffield Hallam University, Sheffield, S1 1WB, UK
[c]Materials and Engineering Research Institute (MERI), Sheffield Hallam University, Sheffield, S1 1WB, UK
[d]Department of Materials and Metallurgical Engineering, Abadeh Higher Education Centre, Shiraz University, Abadeh, Iran
[e]Advanced Materials Research Center, Department of Materials Engineering, Najafabad Branch, Islamic Azad University, Najafabad, Iran

***** Correspondence: tahmadi56@yahoo.com (T.A); rezabakhsheshi@gmail.com (H.R.B.-R.)

Abstract

The present study explores the effect of combined alkaline treatments (NaOH) and the incorporation of functionalized carbon nanotubes (f-CNTs) into poly(lactic acid) (PLA) composite coatings on the corrosion resistance, biocompatibility, and antibacterial efficacy of AZ31 magnesium (Mg) alloy. Various pretreatment techniques and coating layers have been found to exert considerable influence on the phase composition, morphology, thickness, wettability, as well as corrosion resistance, and biological characteristics of the Mg alloy. The formation of an $Mg(OH)_2$ layer on alkaline-treated Mg alloy has proven to enhance hydrophilicity, corrosion resistance, and biocompatibility. Moreover, the findings highlight that incorporating f-CNTs into PLA improves the corrosion resistance, cytocompatibility, and antibacterial activity of Mg alloy in physiological solutions and the extent of these improvements is related to the quantity of f-CNTs present in the composite coating. Additionally, the outcomes have shown that the inclusion of f-CNTs promotes the formation of hydroxyapatite (HAp) during a 14-day immersion in simulated body fluid (SBF). Overall, the combination of alkaline treatments and the PLA/f-CNTs composite coating is showcased as a promising surface modification approach for orthopedic applications.

Keywords: Mg alloys; Alkaline treatments; PLA/f-CNTs composite coating; Corrosion, Biocompatibility; Antibacterial activity

1. Introduction

Magnesium (Mg) alloys exhibit mechanical properties similar to those of natural bone, excellent biocompatibility, and are susceptible to corrosion within the pH range of 7.4–7.6, especially in environments with high chloride concentrations typical of physiological systems [1-3]. The fascinating attributes of Mg alloys have garnered significant interest, particularly in the context of biodegradable bone implant applications [4-6]. In connection with this aspect, a considerable amount of investigations have been carried out on both *in vitro* and *in vivo* corrosion of Mg-based alloys [7-9]. The density and elastic modulus of Mg alloy fall within a comparable range to that of natural human bone. This attribute makes it a promising option as a bone replacement, providing a more pleasant experience in contrast to traditional non-reactive metal biomaterials like stainless steel and titanium alloys. In contrast to these traditional biomaterials, Mg alloy can be assimilated by tissues, making it well-suited for applications in fixation areas. This quality eliminates the necessity for a subsequent surgical intervention once the tissues have completely recovered [10-12].

Nevertheless, the corrosion rate of Mg-based alloys remains relatively high, ranging from 3 to 8 mm/y within the initial 24-hour immersion period in simulated body fluid (SBF), due to the electrochemical activity of Mg [13-16]. Consequently, an untreated Mg-based component undergoes complete degradation within a period of 2 weeks upon immersion. This situation has the potential to lead to the failure of Mg-based implants before the complete healing of the corresponding damaged tissue, and triggering inflammation in surrounding tissues. This poses a challenge to the broader application of Mg-based implants in clinical settings [17-20]. Hence, various approaches have been suggested to improve the corrosion properties of Mg-based alloys [17, 21, 22]. Surface modification is recognized as a potential technique for enhancing the corrosion properties of Mg-based alloys, as it establishes a protective barrier between the metal and its surrounding environment [23-26]. In this context, polymer coating films remain among the most effective surface treatments. Poly(lactic acid) (PLA), sourced from renewable biomass like wheat, corn, or rice, emerges as a highly favorable eco-friendly polymer compared to traditional petroleum-based plastics [27-29]. PLA has been widely employed in various fields, including biomedical materials and biocomposites, owing to its exceptional biodegradability and favorable processing characteristics [30]. Furthermore, owing to its biocompatibility, PLA emerges as a promising material for implant development, given its easy absorption via hydrolytic degradation

processes within the human body. Lactic acid, naturally present in the human body, facilitates the degradation of the polymer, leading to the generation of H_2O and CO_2 through the Krebs cycle [31]. Nonetheless, the intrinsic brittleness and absence of antiradical activity in PLA limit its application in the biomedical fields. To enhance the toughness and antiradical properties of PLA, the addition of nanofillers has been employed [32, 33]. Likewise, the reported issues of PLA surface contamination and the formation of biofilms pose significant challenges for its broader adoption in the biomedical field, as they serve as potential sources of infection [33]. In this context, the incorporation of antibacterial nanofillers is employed to create PLA-matrix composites with antibacterial properties [34, 35]. Gaining prominence in a range of biomedical uses, such as biological diagnosis and drug delivery, the oral delivery of carbon nanotubes (CNTs) continues to be the favored approach for pharmaceutical administration [36, 37]. This selection is made due to its cost-effectiveness, absorbent characteristics, non-invasiveness, and patient comfort [38, 39]. Elimelech *et al.* have reported the bactericidal properties of CNTs against *Escherichia coli* and *Staphylococcus aureus* bacteria. They studied both single-walled carbon nanotubes (SWCNTs) and multi-walled carbon nanotubes (MWCNTs) types of CNTs, in which SWCNTs exhibited a pronounced bactericidal effect, attributed to their smaller tube diameter. Comparable outcomes have been observed for both Gram-negative and Gram-positive bacteria [38-40]. The mechanism likely involves membrane disruption and oxidative stress, which are associated with the chemical and physical characteristics of CNTs [39-43].

Moreover, reports indicate that the functionalization of CNTs through non-covalent association with polymers has been suggested as an effective strategy to enhance their water dispersibility and, consequently, their biocompatibility. Numerous studies by various researchers have illustrated that well-dispersed CNTs are non-toxic to various cell lines and primary cells, such as mesenchymal stem cells. Overcoming this challenge is crucial in the processing or engineering of CNTs because, in their pristine form, they tend to exist as aggregates or bundles held together by hydrophobic interactions between the sp^2 carbon tube shells [39, 40, 43-46]. An earlier *in vitro* investigation has shown that the toxicity of MWCNTs to human cells was notably impacted by the clustering phenomenon. Kang *et al.* discovered that partially unbundled MWCNTs with a diameter of 4.1 μm (achieved through functionalization in a mixture of H_2SO_4 and HNO_3) exhibited greater toxicity towards bacteria in comparison to larger MWCNT bundles with a diameter of 77 μm [40, 47]. Nevertheless, there is limited knowledge regarding the antibacterial efficacy of functionalized

carbon nanotubes (f-CNTs)/PLA-$Mg(OH)_2$ against bacteria. In the course of this investigation, PLA was utilized to coat CNTs, creating PLA/CNTs composites. Consequently, we delved into the electrochemical behavior and antibacterial properties of Mg-based alloy subsequent to anodization in sodium hydroxide (NaOH) alkaline solutions. A comparable study demonstrated the synthesis of a nonstructural film of $Mg(OH)_2$ on the AZ31 Mg alloy substrate using the hydrothermal method. In this process, NaOH solution acted as a mineralizer to decrease the corrosion rate of materials based on Mg. Hence, this initiative is expected to be beneficial in enhancing the corrosion resistance and antibacterial properties of PLA/f-CNTs nanocomposites, and potentially other types of nanocomposites as well.

2. Materials and methods

2.1. Sample pretreatment and coating

The substrate of Mg-based alloy was obtained by machining AZ31 alloy commercial ingots, which were then cut into several specimens with approximate dimensions of 10×10×7 mm^3. Each sample underwent a stepwise polishing process using SiC papers with grit sizes ranging from 800 to 2000. Subsequently, the prepared specimens were cleaned in ethanol and distilled water ultrasonically for 10 minutes each and left to dry at ambient conditions before utilization. As part of the alkaline pretreatment, the Mg alloy samples underwent immersion in a 1 M NaOH solution for 24 h at 75°C. Following this treatment, the samples were cleaned with deionized water, and the resulting sample was labeled as Mg-OH. Following the pretreatment, the samples were washed with distilled water and then dried using warm air. The coating layers of PLA and PLA/f-CNTs were applied to the surfaces of the alkaline-treated samples using the dip-coating method according to Ref. [17]. To reduce the Van der Waals force between CNTs, functional groups like carboxyl (–COOH) and hydroxyl (–OH) were introduced onto the surface of the CNTs. This was accomplished by soaking the CNTs in a solution of H_2SO_4 and HNO_3 with a volume ratio of 1:3 for 4 h at 40°C. The resulting slurry was filtered and subsequently rinsed with both distilled water and ethanol based on Ref. [48]. Solutions of PLA with concentrations of 10 wt.% were formulated by dissolving PLA granules in dichloromethane (DCM) solvent under magnetic stirring for 5 h. Colloids were then created by combining various concentrations (0.1, 0.3, and 0.5 wt%) of f-CNTs with the PLA polymer solution (10 wt%). The resulting colloidal solution underwent continuous stirring for 10 h (Schem. 1). Finally, the prepared samples were immersed in the mixed solutions for 30 seconds and then withdrawn from the solution.

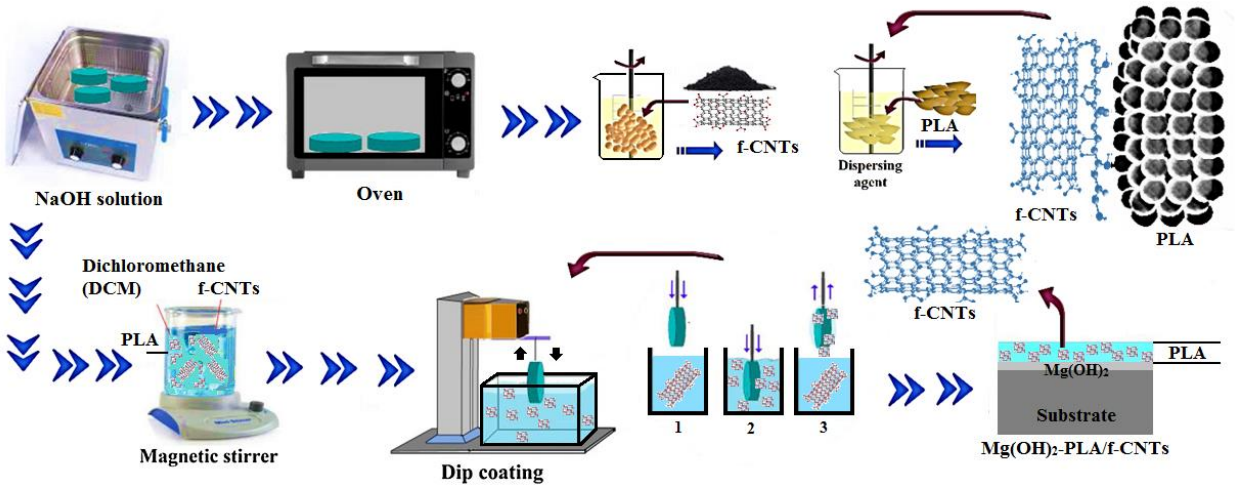

Schem. 1. Schematic illustrating the formulation process for $Mg(OH)_2$-PLA/f-CNTs nanocomposite coating on Mg alloy.

2.2. Characterizations

Microstructures of the samples were analyzed using a Mira3 TE.SCAN field emission scanning electron microscope (FESEM). Phase analysis was conducted using a Bruker D8 X-ray diffractometer. The energy-dispersive X-ray spectrometer (EDS) integrated into the FESEM microscope was utilized for the elemental analysis. X-ray diffraction (XRD) experiments involved Cu–Kα X-ray with a scanning speed of 8° per minute within a 2θ range of 20–80°. The wetting characteristics of the specimens were evaluated using the sessile drop procedure, employing a GBX Digidrop, Romans-sur-Isère (made in France) video contact angle device with a drop size of 10 mL at ambient conditions. Fourier transform infrared (FTIR) spectra were captured employing a Nicolet 5700 spectrophotometer. The outcomes presented are derived from examining three samples within each composite material group.

2.3. Corrosion tests

The measurements of potentiodynamic polarization were conducted on both bare and coated Mg alloys using a Zennium potentiostat from Zahner, Germany. In the electrochemical test, a standard 3-electrode setup was employed, with platinum foil serving as the counter electrode (CE), a saturated calomel electrode (SCE, saturated KCl) as the reference electrode (RE), and the specimen as the working electrode (WE). The potentiodynamic polarization was recorded at a scan rate of 0.5 $mV.s^{-1}$. Electrochemical impedance spectroscopy (EIS) covered a frequency spectrum from 10^5 to 10^{-2} Hz, utilizing a sinusoidal voltage with a 5 mV amplitude. The acquired experimental

data underwent fitting and analysis using the commercial software ZsimpWin 3.50. Each measurement was replicated at least five times to ensure reproducibility. Specimens underwent immersion tests following the ASTM G31-72 standard. Subsequently, the specimens were immersed in a beaker with 200 ml of Ringer's solution at 37 °C. Post-immersion, the surface appearance of corroded specimens was assessed using scanning electron microscopy (SEM) and EDS.

2.4 *In vitro* biocompatibility

Human adipose mesenchymal stem cells (hADSCs) osteoblastic cells were cultured in α-MEM culture media supplemented with 10% FBS and 1% penicillin and streptomycin. Culturing the cell was performed in a humidified environment having 5% CO_2 at 37 °C, and the culture media were replenished every 48 h. When the cells reached 80 to 90% confluency, they were detached utilizing 0.25% trypsin/EDTA and then sub-cultured at a density of 10^5 cells per cm^2 in a 100 mm petri dish. Cells from the 3rd-6th passage of hADSCs were utilized for the tests. All cell assay experiments were performed in triplicate for every sample type at every time point, and the experiments were repeated at least once. The cell viability assay was conducted employing an indirect contact technique. The hADSCs were seeded in a 96-well plate at a density of 2×10^4 cells per mL with 100 µL of suspension for every well and incubated for 24 h to allow attachment. Subsequently, the culture media were replaced with 100 µL of the sample extracts. Following the incubation, for all time points of 1, 3, and 5 days, 10 µL of CCK8 solution was added to each well and incubated for 2 h in a cell incubator. The optical density (OD) was then measured at 450 nm using an iMARK (Bio-Rad, USA) microplate reader according to Ref. [49].

2.5 Antibacterial activity test

The plate counting technique was utilized for the evaluation of bacterial growth on both untreated and treated samples. The coated samples were subjected to sterilization using UV light and were placed in a sterile Petri dish. Subsequently, 100 µL of culture media containing 5×10^5 CFU/mL of *Staphylococcus aureus (S. aureus)* bacteria was applied to the surfaces of the samples. Afterwards, the samples were incubated at 37 °C for 1 h, and their surfaces were rinsed with a saline solution to retrieve the proliferated bacteria. The collected suspensions underwent a fourfold dilution and were then plated on agar-agar (TSA, Becton-Dickinson, Sparks, MD, USA) plates, which were incubated at 37 °C for 24 h. Following the incubation period, a light microscope was utilized to

count the colonies formed on every plate, thereby evaluating the antibacterial effectiveness of the specimens against *S. aureus* bacteria.

2.6. Statistical analysis

The results obtained in this study were presented as the mean ± standard deviation, calculated from a sample size of n = 3. Statistical significance was evaluated through one-way analysis of variance (ANOVA), and $P < 0.05$ was deemed as the significance threshold.

3. Results and discussion

3.1. Characterization

Fig. 1 shows the SEM micrographs of the initial powders used for $Mg(OH)_2$, PLA, and PLA/f-CNTs coatings. In the case of alkaline-treated (AB1) samples, it is noticeable that extensive overlapping flakes appear in a disordered manner on the surface of AB1 specimen, exhibiting the characteristic morphology of $Mg(OH)_2$ under similar reaction conditions. It is important to highlight that the surface of AB1 specimen consists of compact nanoparticles, with a predominantly dense surface, yet some micropores of irregular sizes are detectable. These micropores could have a notable impact on the corrosion behavior of the samples. The PLA coating (AB2) displayed a surface that was smooth with cracks and featured some small nodules. However, the incorporation of f-CNTs into the PLA matrix resulted in the emergence of a highly flake-like morphology (AB5). The micrograph illustrates that in the PLA/f-CNTs coating with varying filler amounts, f-CNTs are dispersed relatively uniformly within PLA, without distinct regions rich in isolated f-CNTs. In the PLA/f-CNTs coating with a higher concentration of f-CNTs, the tips of incorporated f-CNTs can serve as nucleation sites within the matrix [50]. Additionally, the cross-section of the PLA/0.3f-CNTs nanocomposite coating (AB4) reveals the formation of a substantial layer of $Mg(OH)_2$-PLA/0.3f-CNTs, with a thickness of about 58.5 μm, that uniformly covers the surface of the bare nanocomposite. This comparatively high-thickness layer reduces the corrosion rate by acting as an impediment to metal dissolution. It is noteworthy that the incorporation of varying amounts of f-CNTs into the PLA layer has minimal impact on the film thickness. Importantly, when the substrate is exposed to a corrosive solution, the protective efficacy is improved by incorporating a layer with increased thickness and density. Thus, it can be deduced that there is a direct correlation between the thickness of the coating and the effectiveness of protection.

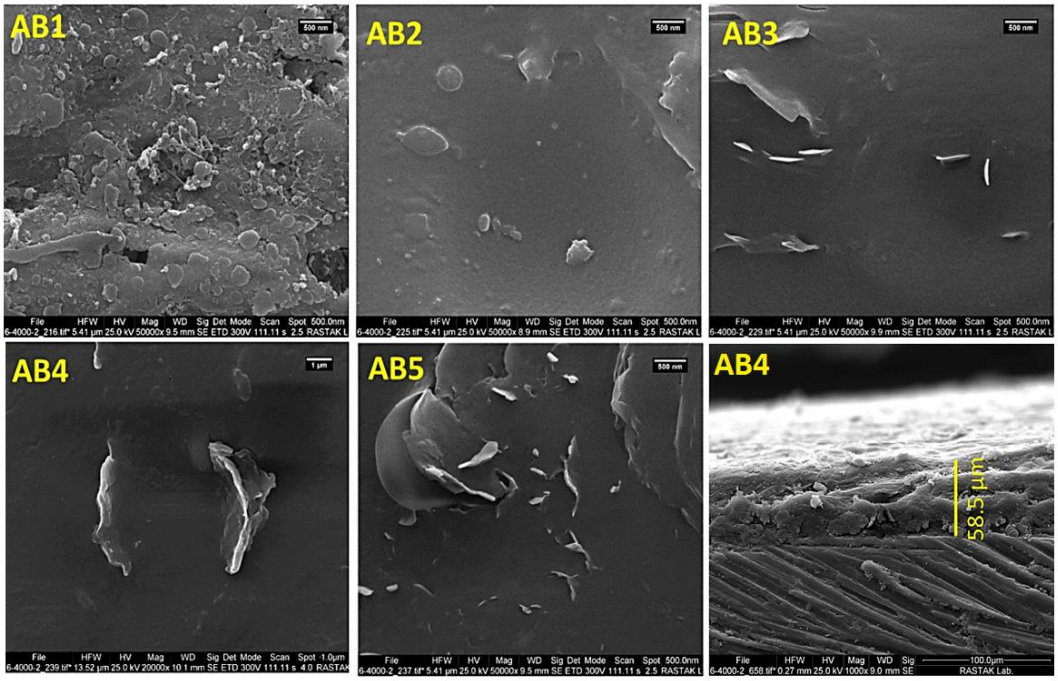

Fig. 1. FESEM micrographs depict the surfaces of alkaline-treated (AB1), PLA (AB2), PLA/0.1f-CNTs (AB3), PLA/0.3f-CNTs (AB4), and PLA/0.5f-CNTs (AB5) composite coatings. Additionally, a cross-sectional image of the PLA/0.3f-CNTs (AB4) composite coating sample is included

In Figs. 2A, and 2B, the XRD patterns of the untreated AZ31 alloy, $Mg(OH)_2$, PLA, and PLA/f-CNTs coating samples are presented. The XRD pattern of the alkaline treatment (AB1) sample reveals that the primary phase of the alkaline pretreatment was $Mg(OH)_2$, consistent with findings from earlier investigations [15,25]. Nevertheless, only the diffraction peaks of Mg (JCPDS No. 35-0821) are evident in the XRD pattern of the uncoated Mg alloy [17]. The XRD analysis reveals two prominent peaks at 16.5° and 19° in the specimens. These two peaks indicate the diffraction of (110)/(200) and (203) crystal planes of PLA/f-CNTs, respectively [50]. It is important to mention that other peaks of f-CNTs are not observed, likely due to their low content, falling below the detection limit of the XRD instrument.

The outcomes of the investigation into the presence and characteristics of interfacial interactions are depicted in Figs. 2C and 2D, showcasing the FTIR patterns of the Mg alloy, $Mg(OH)_2$, PLA, and PLA/f-CNTs coatings. Notably, no peaks were seen on the original Mg alloy, revealing the absence of chemical groups on the surface. Following alkaline treatment, a robust absorption peak appeared at about 3700 cm^{-1}, corresponding to the characteristic peak of hydroxyl groups. This suggests the formation of a protective passive layer with an increased number of hydroxyl groups [10]. In Figs. 2C and 2D, the acquired FTIR spectra reveal three distinctive absorption bands:

2918, 1749, and 1181 to 1083 cm^{-1}, corresponding to the stretching vibrations of –OH, C=O, and C–O groups of PLA, respectively. Additionally, a bending vibration of CH_3 groups is observed at 1456 cm^{-1}, and at 1379 to 1362 cm^{-1} (not denoted), bands arise from the C–H deformation and asymmetric/symmetric bending, respectively. The bands at 868 and 758 cm^{-1} correlate to the bending vibration of C=C and C–H groups, respectively [34]. The FTIR spectra of PLA/f-CNTs samples did not exhibit a characteristic vibration of intermolecular –OH (3550 to 3200 cm^{-1}). However, a weak vibration at 2918 cm^{-1} correlated to the existence of intramolecular –OH was seen in both PLA and PLA/f-CNTs. Additionally, a band at 1210 cm^{-1} in PLA/f-CNTs may be attributed to the stretching vibrations of C-O bonds. Moreover, the stretching vibrations of C-O groups from PLA at 1083 cm^{-1} shifted to a lower wavenumber for PLA/f-CNTs. This suggests that the adhesion mechanism between f-CNTs and the PLA matrix might be associated with an interaction of terminal hydroxyl groups of PLA, included in carboxyl groups, with hydroxyl groups on the CNTs surface via a condensation reaction [34]. It is noteworthy that groups of f-CNTs exhibit peaks at 1631 cm^{-1} and 2852 cm^{-1}/2923 cm^{-1}, relating to the C=C and C–H vibrations, respectively. Two new bands are observed, representing the vibrations of C=O at 1661 cm^{-1} and O–H at 920 cm^{-1}/1430 cm^{-1}, arising from the carboxylic (–COOH) groups [33, 34]. These findings indicate the successful introduction of oxygenic functional groups after HNO_3/H_2O_2 treatment. Similarly, a characteristic band was observed in the PLA/f-CNTs coating containing a higher amount of f-CNTs.

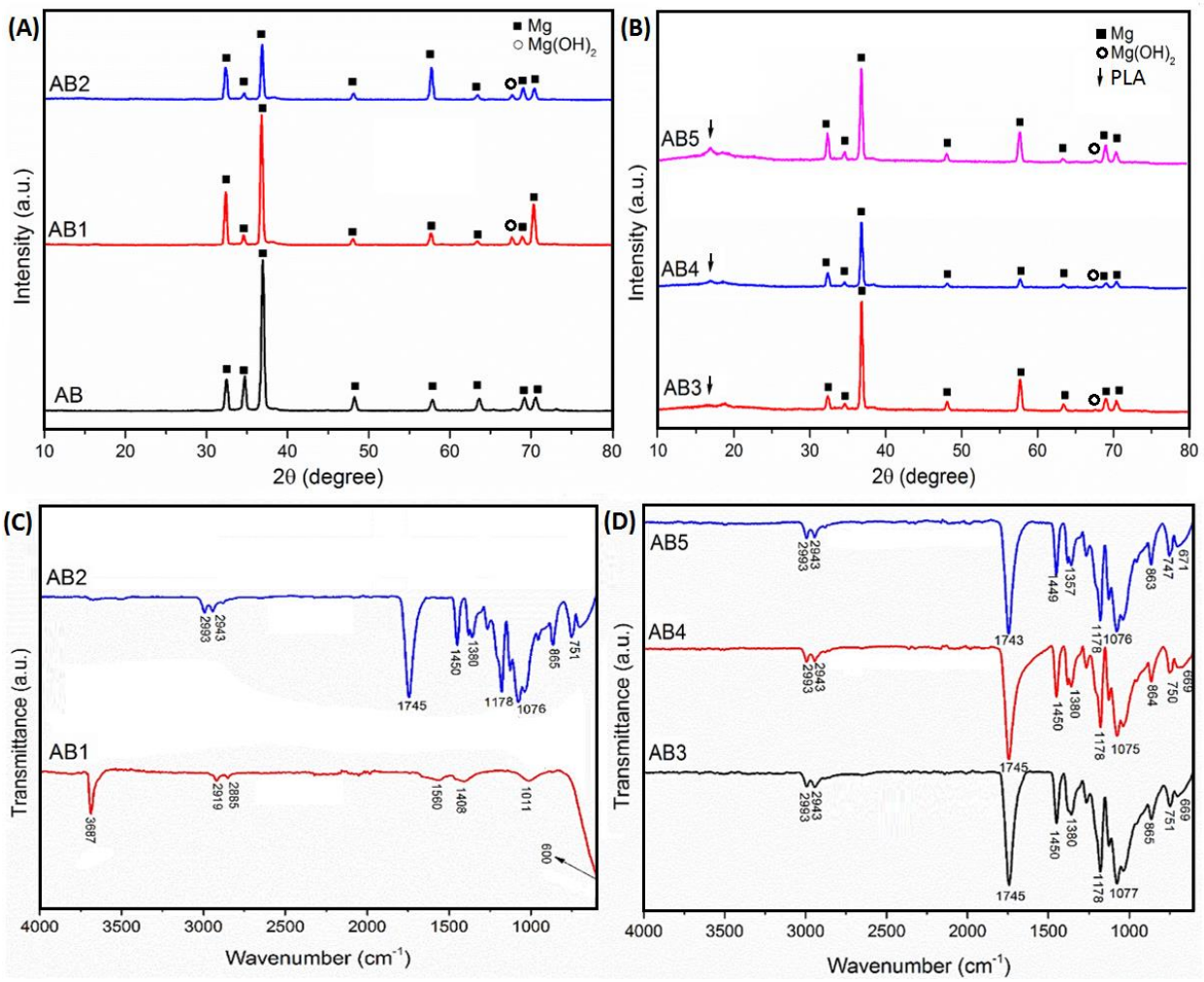

Fig. 2. (A, B) XRD patterns, (C, D) FTIR analysis of uncoated (AB), alkaline-treated (AB1), PLA (AB2), PLA/0.1f-CNTs (AB3), PLA/0.3f-CNTs (AB4), and PLA/0.5f-CNTs (AB5) composite coatings.

3.2. Water contact angle

The microstructure and chemical composition of a material's surface are recognized as influential factors in in-vitro bioactivity within aqueous environments. Consequently, surface properties, including surface free energy and wettability, play a vital role in determining the biological performance of materials [10]. In this context, water contact angle (WCA) measurements were conducted to assess surface wettability. As depicted in Fig. 3, a noticeable decrease from 70.8° for the pristine Mg to 51.4° was observed after alkaline treatment. This reduction can be correlated to the introduction of a large number of –OH groups on the Mg alloy surface during treatment, facilitating the formation of hydrogen bonds and resulting in enhanced hydrophilicity [10, 51]. Additionally, it was observed that the WCA for the PLA coating was 87.3°. With an increase in the f-CNTs content to 0.1 and 0.5 wt% in the composite coating, a slight decrease in the WCA was

noted. This reduction in the WCA may be attributed to the presence of interconnecting f-CNTs particles within the PLA matrix [44]. The incorporation of f-CNTs significantly enhanced the hydrophilic properties of the PLA-based coating, primarily attributed to the hydrophilic nature of f-CNTs containing a substantial number of oxygenated functional groups [10, 52]. It's noteworthy that the WCA remained smaller than that of the PLA coating even with the introduction of hydrophilic carboxyl groups. A consistent trend of decreased WCA was observed with the incorporation of f-CNTs, indicating a continuous enhancement of hydrophilicity by encapsulating f-CNTs in the PLA matrix.

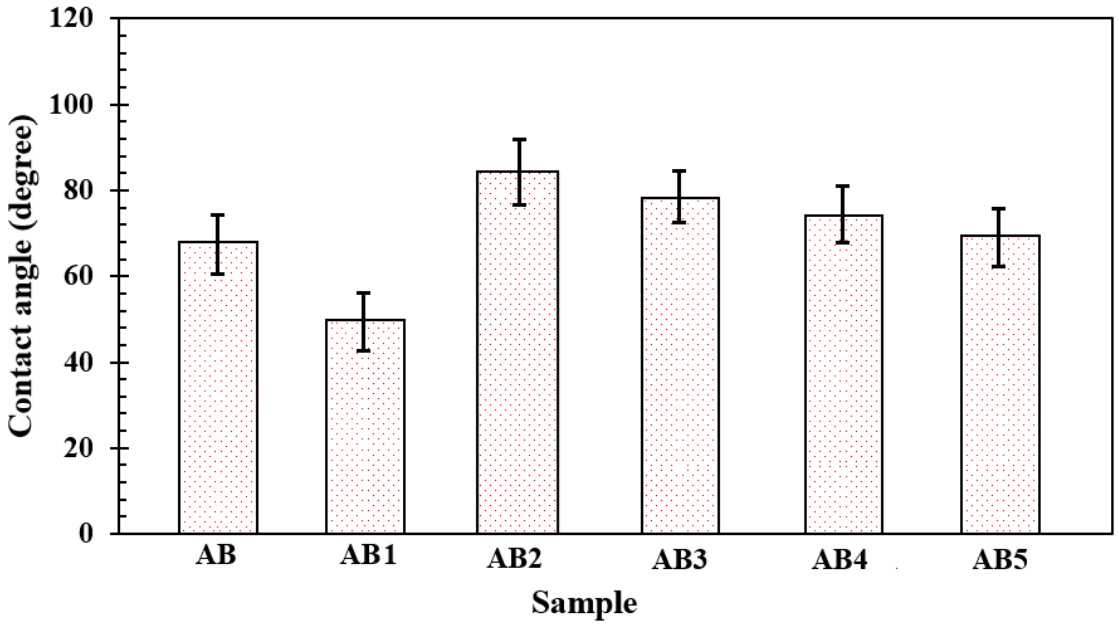

Fig. 3. Results of WCA measurements for (AB), alkaline treated (AB1), PLA (AB2), PLA/0.1f-CNTs (AB3), PLA/0.3f-CNTs (AB4) and PLA/0.5f-CNTs (AB5) composite coatings

3.3. Corrosion studies

Figs 4A, and 4B present the Tafel polarization curves of AZ31 Mg-based substrate and the treated specimens after a 15-minute soaking in Ringer's solution at 37 ± 1°C. Also, the electrochemical parameters derived from the Tafel polarization curves for each sample are tabulated in Table 4. Initially, it is notable that the corrosion current density (i_{corr}) of all the treated samples has shifted to more negative values compared to the AZ31 Mg alloy. It can be deduced that after alkaline treatment, the i_{corr} declined, which indicates an enhancement in the corrosion properties of the Mg-based alloy. Forming a magnesium hydroxide layer on the surface of AZ31 Mg alloy led to a reduction in current density and an increase in corrosion resistance. Furthermore, PLA/f-CNTs coatings with lower f-CNTs content exhibited superior corrosion resistance compared to their

counterparts with higher f-CNTs content. The presence of a smaller amount of CNTs decreases the dynamic and kinetic inclination towards corrosion, as evidenced by the i_{corr} values. Regarding the effect of CNTs, their presence in the coatings enhances the barrier effectiveness in resistance to the corrosive solution compared to PLA coating alone. This enhancement can be attributed to the bridging mechanism of CNTs within the PLA matrix, creating a more compact coating structure that restricts the access of the corrosive solution to the base material [32, 53-55]. However, increasing the CNTs content up to 0.5 wt.% in the composite coatings leads to an elevated corrosion rate. This could be attributed to the non-uniform coating morphology of PLA/0.5f-CNTs samples, possibly caused by the agglomeration of CNTs. In this context, the polarization resistance (R_p) associated with the PLA/0.3f-CNT (4.17 $k\Omega.cm^2$) was significantly higher than that of PLA (2.25 $k\Omega.cm^2$) and PLA/0.5f-CNTs (1.03 $k\Omega.cm^2$). This difference is possibly attributed to the higher thickness of the dense barrier layer [40], resulting in enhanced corrosion protection in the f-CNTs reinforced PLA coating than the PLA coating without f-CNTs, as presented in Table 1. Moreover, it can be inferred that the diffusion resistance of the dense barrier layer primarily contributes to the corrosion protection of the coating system.

Figs. 4C, and 4D depict the Nyquist diagrams corresponding to untreated Mg alloy, $Mg(OH)_2$, PLA, and PLA/f-CNTs coatings samples in Ringer's solution. In the figure, all the curves of the samples exhibit a capacitive semi-circle, indicative of load transfer resistance. As evident, the untreated sample displays a capacitive semi-circle with the smallest radius, while alkaline treatment on the sample surface increases the diameter of the capacitive semi-circles to 2054 $\Omega.cm^2$. This suggests that the formation of the $Mg(OH)_2$ layer on the Mg alloy surface has enhanced its corrosion resistance. Comparing the diameters of semi-circles related to PLA/f-CNTs coated and uncoated samples in Figs. 4C and 4D show not only a remarkable enhancement in the corrosion behavior of AZ31 alloy but also the prevention of local corrosion. Additionally, a preliminary comparison between the Nyquist diagrams of PLA and PLA/0.3f-CNTs suggests that PLA/0.3f-CNTs provide higher protection in comparison with PLA for both immersion times. Building upon the prior discourse, a proper equivalent electrical circuit was used for the fitting of individual data series. Instead of an ideal capacitor, a constant phase element was utilized to account for non-ideal characteristics associated with surface irregularities and/or roughness.

In this context, R_s, CPE, and CPE_{dl} represent the resistance of the solution, constant phase element, and double-layer capacitance, respectively. On the other hand, R_{ct} and R_{pore} denote the resistance

to charge transfer and resistance in the pores of the surface film. The PLA/0.3f-CNT (Rct: 14120 $\Omega.cm^2$) exhibits significantly higher resistance than PLA/0.5f-CNTs (Rct: 3623 $\Omega.cm^2$), possibly attributed to the absence of agglomeration and the compact nature of the PLA-coated film containing f-CNTs, as presented in Table 2. Conversely, uncoated and alkaline-treated samples show lower corrosion resistance due to lower thermodynamic stability and the formation of a thin film with less compactness of $Mg(OH)_2$.

The analysis of Bode modulus curves in Figs. 4E and 4F reveal that PLA/0.3f-CNTs coated sample exhibits the highest impedance modulus at low frequencies, confirming its superior resistance to aggressive ions. Moreover, the PLA/0.3f-CNTs coating layer proves to be more effective in inhibiting the corrosion phenomenon in the substrate. Additionally, the phase angle at the highest frequency (–Θ) serves as a relevant parameter for assessing the corrosion resistance of the uncoated and PLA-coated specimens containing f-CNTs, as derived from the phase plots presented in Figs. 4E and 4F. The –Θ value for the PLA/0.3f-CNTs coating experiences a significant decrease from approximately 62º to about 58º for PLA/0.1f-CNTs and 43º for PLA/0.5f-CNTs. Meanwhile, the –Θ values for PLA with a low amount of CNTs undergo minor changes, underscoring the role of f-CNTs in the PLA matrix in maintaining the barrier performance of the PLA/f-CNTs composite coating. Consequently, it can be deduced that the primary factor contributing to the reduction in the corrosion rate of the substrate is the mass transfer resistance of the corrosion products layer.

Table 1. Electrochemical parameters of samples in SBF solution obtained from the polarization experiment

Samples	β_a ($v.dec^{-1}$)	$-\beta_c$ ($v.dec^{-1}$)	E_{corr} (V)	i_{corr} ($\mu A/cm^2$)	R_p ($k\Omega.cm^2$)
AB	0.051	0.261	-1.55	19.05	0.97
AB1	0.054	0.385	-1.49	19.95	1.03
AB2	0.061	0.496	-1.54	10.47	2.25
AB3	0.048	0.378	-1.52	8.12	2.28
AB4	0.055	0.323	-1.61	4.89	4.17
AB5	0.073	0.357	-1.58	19.67	1.34

Table 2. Outcomes of Fitting of impedance experiment on the electrochemically equivalent circuit

Samples	R_s ($ohm.cm^2$)	CPE_{dl} ($S.sec^n/cm^2$)	n	R_{ct} ($ohm.cm^2$)
AB	10.6	3.63E-5	0.80	812
AB1	145.2	5.73E-6	0.78	2054
AB2	146.7	6.54E-6	0.74	6583
AB3	104.2	3.38E-6	0.82	7500
AB4	236.4	2.30E-6	0.57	14120
AB5	28.87	3.86E-5	0.69	3623

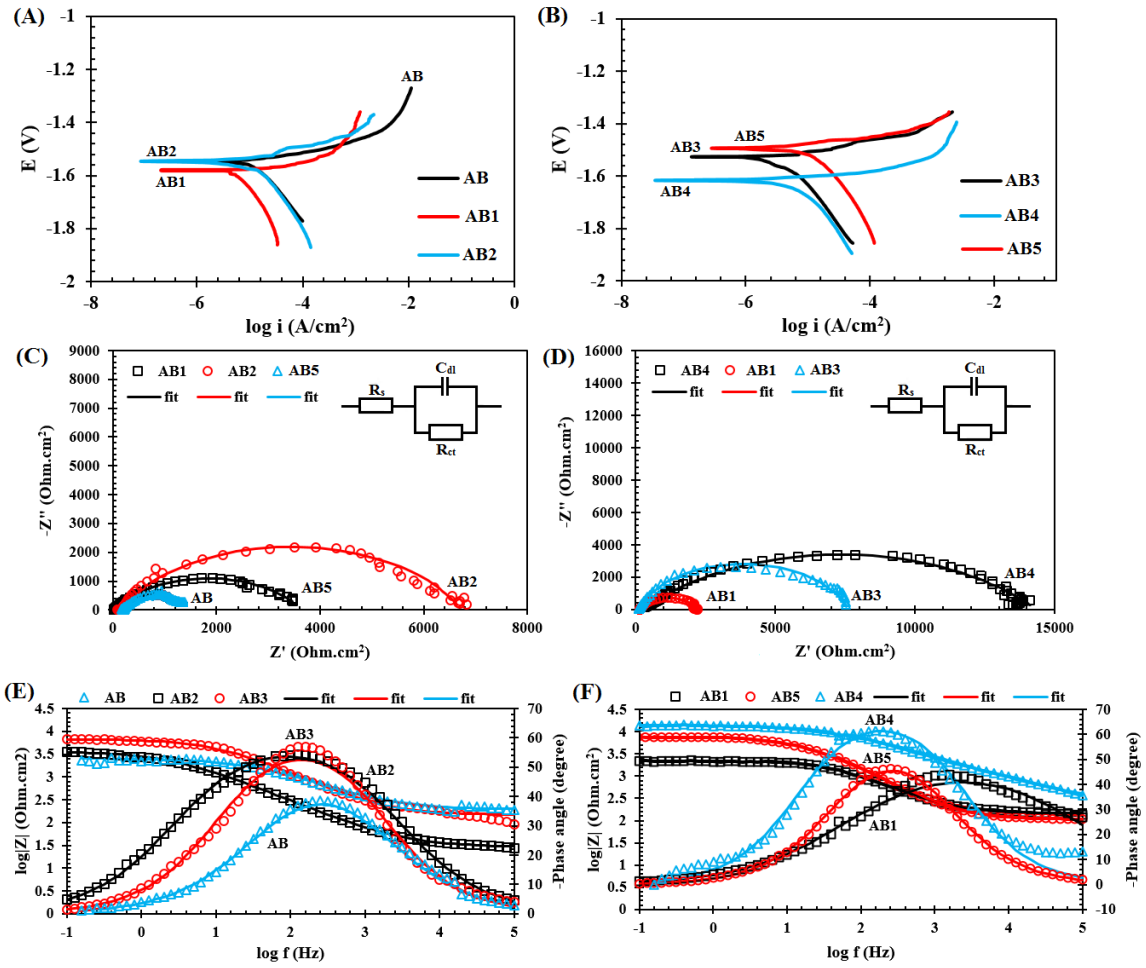

Fig. 4. (A, B) Polarization curves, (C, D) Nyquist curves, and (E, F) Bode modulus and Bode phase plots of for uncoated (AB), alkaline treated (AB1), PLA (AB2), PLA/0.1f-CNTs (AB3), PLA/0.3f-CNTs (AB4) and PLA/0.5f-CNTs (AB5) composite coatings

To validate the conclusions drawn from potentiodynamic polarization and EIS studies, an immersion test was conducted on bare and coated Mg-based samples. SEM images of the specimens taken after 14 days of soaking in Ringer's solution are presented in Fig. 5. The surface of the uncoated Mg alloy is covered with corrosion products, along with a large number of pits and cracks, while a partial area of the corrosion products covers the surface of the alkaline-treated Mg alloy [10, 56]. In this context, pitting corrosion occurred for Mg-OH samples, but it was remarkably smaller than that of the uncoated AZ31 alloy. This observation further confirms that a barrier layer of $Mg(OH)_2$ was formed after alkaline treatment. This barrier layer can isolate the Mg matrix from the corrosion in the medium to some extent, contributing to the enhanced corrosion resistance. The morphology of the PLA/f-CNT coating reveals aggregation, with a combination of spherical and irregular structures in regions with lower f-CNT content. The f-CNTs

may agglomerate in certain areas, creating additional nucleation sites. However, in regions with higher f-CNT content, there is a transformation of some corrosion product regions from spherical to plate shape, leading to structural heterogeneity in PLA with increased f-CNT content [48, 54]. SEM images additionally illustrate that the f-CNTs enhance the nucleation sites of hydroxyapatite (HAp) after the application of alkaline treatment following deposition. The increased HAp nuclei may decrease and fill the passageways in the composite coatings, preventing Ringer's solution from penetrating into the substrate. However, the high incorporation of f-CNTs reduced corrosion resistance because of the clustering of CNTs and the decreased homogeneity of the PLA/0.5f-CNTs coatings. The incorporation of CNTs and graphene can concurrently improve the structural integrity and bioactivity of metallic biomaterials, as demonstrated by Zanello *et al.* [57]. They explored the interaction between osteoblast cells and CNT, concluding that CNTs promote the growth of osteoblast cells, leading to subsequent new bone formation [43]. Additionally, previous studies have indicated that the bioactivity of CNTs is largely attributed to their presence, which accelerates bone growth, and biomineralization, and inhibits osteoclastic bone resorption [58]. The enhanced bone repair is facilitated by CNTs stimulating osteoblast proliferation and adhesion [43, 59]. Furthermore, CNTs can serve as an efficient nano matrix for the growth of HAp crystals with stoichiometric values aligned with natural HAp [60-62]. As a result, CNTs serve as an effective nucleation surface, promoting the formation of a biomimetic apatite coating [63]. Additionally, in coatings with added CNTs, the newly deposited layer covers the pre-existing layer. This observation suggests that the increase in nucleation sites, facilitated by f-CNTs, can compensate for the low concentration of calcium and phosphate ions, leading to a reduction in the nucleation formation energy of new deposits. Furthermore, the higher specific area of CNTs allows for more sites for the absorption of Ca^{2+}, PO_4^{3-}, and OH^- ions from the SBF solution, leading to the formation of a new Ca-P layer [54].

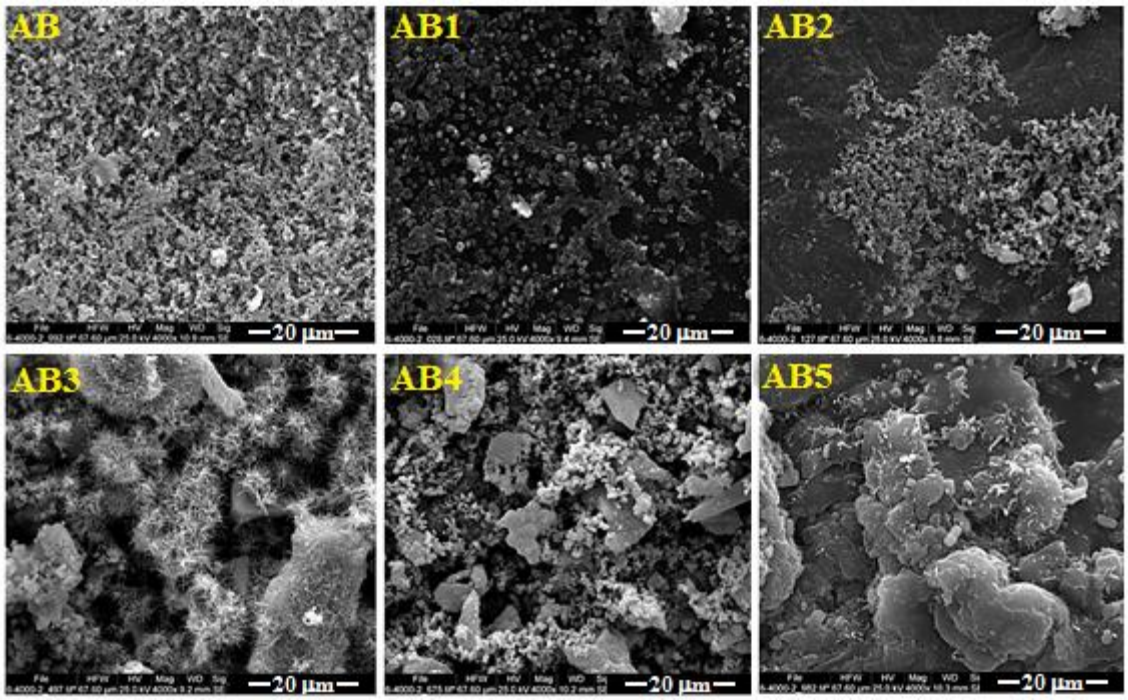

Fig. 5. FESEM micrographs of uncoated (AB), alkaline treated (AB1), PLA (AB2), PLA/0.1f-CNTs (AB3), PLA/0.3f-CNTs (AB4) and PLA/0.5f-CNTs (AB5) composite coatings after a 14-day immersion in SBF solution.

Fig. 6 provides additional insights into the morphology and EDS spectra of the Mg alloys and PLA/f-CNTs composite coating sample after a 14-day immersion in Ringer's solution. EDS surface analysis conducted on the top view of the uncoated and PLA/f-CNTs composite coating can trigger $Mg(OH)_2$ and $MgCO_3$ formation during immersion in the Ringer's solution. EDS precipitation mapping results revealed the existence of Mg, O, C, P, and Cl on the surfaces of both the uncoated and PLA/f-CNTs composite-coated samples. The composite coated samples displayed a more evenly distributed surface composition of O, C, Na, and P with a lower amount of Cl compared to the uncoated samples. The consistent distribution of carbon verified the existence of f-CNTs in the PLA/f-CNTs composite. Oxygen (O) is derived from Mg degradation reactions in the Ringer's solution. When comparing the element mappings of Mg and O, it was noticed that regions abundant in Mg corresponded with regions rich in O, suggesting the formation of magnesium hydroxide ($Mg(OH)_2$) on the surface of the Mg-based composite specimen during immersion in Ringer's solution.

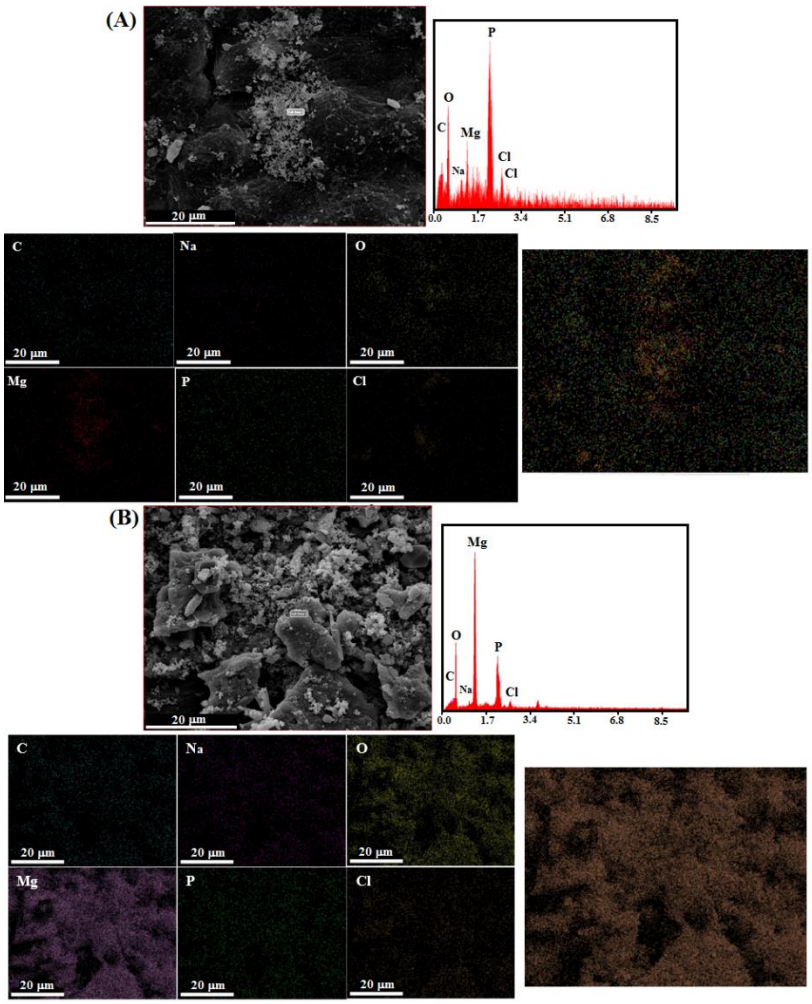

Fig. 6. FESEM micrographs and EDS analyses of (A) uncoated Mg specimen, and (b) PLA/0.5f-CNTs composite coatings after 14 days of immersion in SBF solution.

3.4. Antibacterial activities

The antibacterial activities of untreated Mg alloy, $Mg(OH)_2$, PLA, and PLA/f-CNTs coated samples with different concentrations of f-CNTs were assessed using the colony counting method against *Staphylococcus aureus* (*S. aureus*) as a bacterial model. The antibacterial performance of all samples is illustrated in Fig. 7. Notably, after approximately 24 h of incubation, the as-prepared PLA/f-CNTs coatings with a high f-CNTs concentration exhibited robust antibacterial activity compared to the coatings with a low f-CNTs concentration. By comparing the abundance of colonies on the surface in the images of the figure, it can be inferred that the PLA/f-CNTs coatings with a high f-CNTs concentration led to a slight decrease in the growth of this bacterium, by approximately 10%. The untreated Mg alloy, $Mg(OH)_2$, and PLA samples showed less significant antibacterial activity under the test conditions, as depicted in the figure. The enhanced antibacterial

efficacy of the PLA/f-CNTs coatings is likely attributed to the well-dispersed f-CNTs encapsulated into the matrix of PLA. In this context, f-CNTs function as nano-darts within the solution, consistently targeting the bacteria. This process degrades the bacterial cell integration, ultimately resulting in cell death. Therefore, the antibacterial efficacy of f-CNTs can be significantly enhanced by augmenting the physical puncture of bacteria by f-CNTs. This suggests that cell death is not primarily attributed to the inhibition of cell growth and oxidative stress. Increasing the concentration of f-CNTs raises the population density of nano-darts, consequently improving the antibacterial activity of PLA/f-CNTs coatings [37, 40].

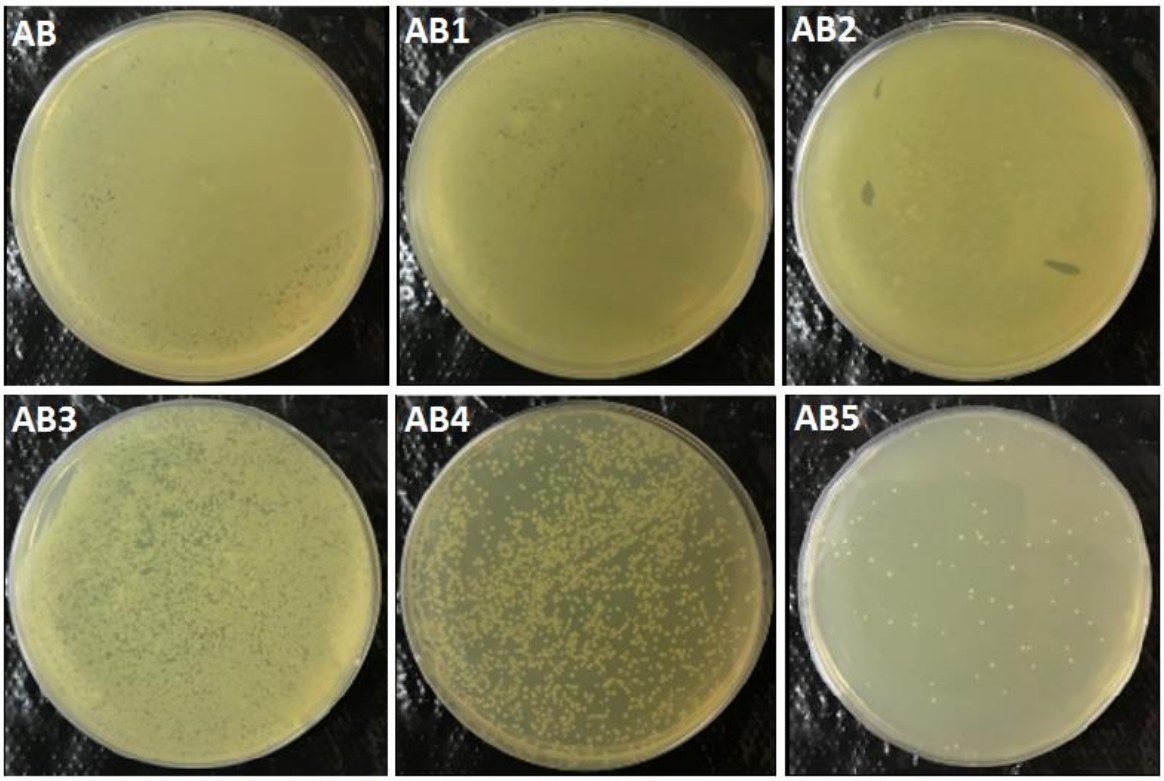

Fig. 7. Antibacterial experiment photograph of colony counting method against *S. aureus* bacterium for uncoated (AB), alkaline treated (AB1), PLA (AB2), PLA/0.1f-CNTs (AB3), PLA/0.3f-CNTs (AB4) and PLA/0.5f-CNTs (AB5) composite coatings

3.5. *In vitro* biocompatibility

To evaluate cell viability, a CCK-8 assay was conducted, and the outcomes are depicted in Fig. 8A. The treated samples with the modified surface exhibited increased cell viability compared to the AZ31 alloy, indicating that endothelial cells could grow and proliferate more effectively on the treated specimens. The addition of a large quantity of –OH groups on the surface through alkaline treatment improved hydrophilicity, leading to higher values [10, 64]. The results show that the

number of cells that grew on the alkaline-treated, PLA-coated, and PLA/f-CNTs-coated specimens increased in a time-dependent manner. The cell viability on the PLA/0.3f-CNTs scaffold was slightly better than that on the PLA and PLA/0.5f-CNTs coatings during the entire culture period. In particular, after 72 h of culture, the OD value for the PLA/0.3f-CNTs coating was higher than that of the uncoated, alkaline-treated, and PLA-based coated samples. The advantageous rod-shaped morphology and nanoscale dimensions of CNTs offer a morphological resemblance to key structural proteins found in the body, such as fibrillar proteins within the extracellular matrix (ECM) [43]. Furthermore, the enhancement of biocompatibility in CNTs is achieved through their interaction with proteins, rendering them non-toxic. The primary adsorption mechanism for proteins onto CNT surfaces involves π–π stacking driven by robust van der Waals forces. This stacking predominantly occurs between the sturdy sp^2 bonding of carbon atoms in carbon nanomaterials and the benzene rings present in amino acids, the fundamental components of proteins. A notable illustration involves bone morphogenetic protein (BMP), a widely recognized protein known for promoting the osteogenic differentiation of metallic implants [43].

Studies have indicated that f-CNTs possess the ability to traverse cell membranes and amass within the cytoplasm, without displaying any harmful effects on the cells [43, 65]. Research conducted by Chen *et al.* [66] proposes that the positive impact on diminishing the cytotoxicity of CNTs is attributed to the adsorption and binding of blood proteins [43]. However, the incorporation of 0.5wt% f-CNTs into PLA-based coated samples had an adverse effect on cell viability, suggesting that composite coatings with high f-CNT content may have adverse impacts on the attachment, spreading, and proliferation of osteoblasts. This could be attributed to the release of a high amount of CNTs, causing alterations in the cellular-level physiological environment, potentially damaging cell membranes, and accumulating in unfavorable positions inside cellular structures [43].

When biomaterials are implanted into the body, surrounding cells undergo changes in morphology, including cell adhesion and spreading [10]. To assess *in vitro* cytocompatibility, direct cell adhesion assays were conducted using hADSC on $Mg(OH)_2$, PLA/0.3f-CNTs, and PLA/0.5f-CNTs samples. The cell adhesion densities and morphologies after 1 day and 3 days of culture are depicted in Fig. 8A. SEM images of adherent cells reveal cell density and morphology on different samples, as shown in Fig. 8B. Over the culture period, there is an overall trend of enhanced attachment of cells on pre-treated and coated Mg-based substrates. The PLA containing f-CNTs exhibits a similar adherent cell density throughout the complete incubation duration, with

significantly more adherent cells on the PLA/0.3f-CNTs specimen than samples containing f-CNT, indicating superior cytocompatibility of PLA/0.3f-CNTs. Furthermore, while hADSC on $Mg(OH)_2$ and PLA/0.5f-CNTs show a roundish and poorly spread morphology subsequent to incubating, cells grown on PLA/0.3f-CNTs samples appear well spread out, with clearly visible filopodia. Overall, fewer cells were seen on the uncoated Mg-based alloy and Mg-OH specimens, while relatively more cells adhered to PLA and PLA/0.3f-CNTs coated samples. The polymer-containing f-CNTs coating contributed to the protection of the substrates, creating a favorable environment for cell attachment and proliferation [67-73]. The f-CNTs and graphene have demonstrated outstanding adherence of extracellular and serum proteins upon exposure to *in vitro* conditions, promoting cell attachment to these nanomaterials.

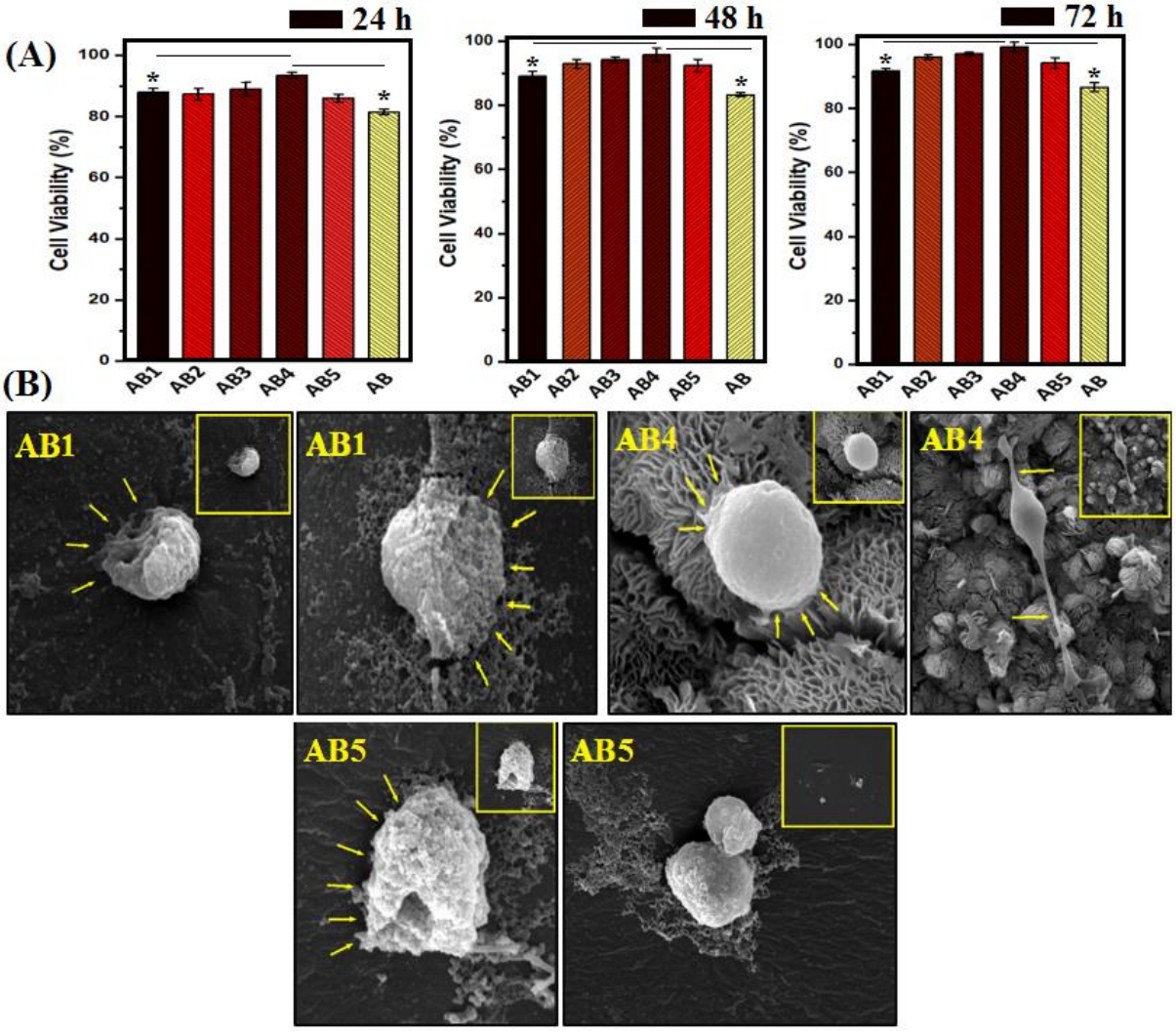

Fig. 8. (A) cell viability, and (B) SEM image of hADSC adhesion for different times on uncoated (AB), alkaline treated (AB1), PLA (AB2), PLA/0.1f-CNTs (AB3), PLA/0.3f-CNTs (AB4) and PLA/0.5f-CNTs (AB5) composite coatings (*$p < 0.05$).

5. Conclusions

In the present work, a combination of alkaline treatments and a composite coating containing $Mg(OH)_2$ and PLA/f-CNTs was successfully made on the Mg-based AZ31 alloy. Alkaline treatments resulted in the formation of the $Mg(OH)_2$ film on the Mg-based alloy surface and introduced a large amount of hydroxyl groups. The results indicated that alkaline treatments led to a notable enhancement in the hydrophilicity (as indexed by the water contact angle, WCA) of the AZ31B Mg-based alloy, while a slight increase in hydrophobicity was observed after applying the PLA/f-CNTs composite coating. Also, it was observed that the composite coatings effectively provided corrosion protection for the Mg-based alloy substrate. Additionally, the findings showed that the PLA/0.3f-CNTs composite coating demonstrated the lowest corrosion current density (icorr) in comparison to other composite coatings with varying concentrations of f-CNTs, signifying its outstanding corrosion resistance. Moreover, the MTT assay demonstrated that the alkaline-treated Mg-based alloy exhibited acceptable cytocompatibility for human adipose mesenchymal stem cells (hADSC). Particularly, the PLA/0.3f-CNTs composite coating successfully improved cell viability, cell attachment, and growth of AZ31 alloy. The research demonstrated that PLA/f-CNTs composite coatings with elevated concentrations of f-CNTs exhibit greater antibacterial activities compared to coatings with lower concentrations, particularly against *S. aureus* bacteria. The f-CNTs act as nano-darts moving within the solution, which can actively attack bacteria. This mechanism results in the breakdown of bacterial cell integrity, ultimately leading to cell death. Moreover, the results showed that uncoated and alkaline-treated Mg-based alloy presented less significant antibacterial activities compared to the PLA/f-CNTs composite coated samples. The approach to surface modification presented in this study not only provides insights into enhancing the corrosion resistance of Mg-based alloys but also achieves favorable antibacterial activity and cytocompatibility with hADSCs, broadening the potential applications of Mg-based alloys in biomedical contexts.

Abbreviations

ANOVA	Analysis of variance	Mg	Magnesium
ASTM	American society for testing and materials	MTT	(3-[4,5-dimethylthiazol-2-yl]-2,5 diphenyl tetrazolium bromide)
BMP	Bone morphogenetic protein	MWCNT	Multi-walled carbon nanotube
CE	Counter electrode	OD	Optical density
CFU	Colony-forming unit	PLA	Poly(lactic acid)
CNT	Carbon nanotube	R_{ct}	Charge transfer resistance

CPE	Constant phase element	RE	Reference electrode
CPE_{dl}	Double layer capacitance	R_p	Polarization resistance
DCM	Dichloromethane	R_{pore}	Pore resistance
ECM	Extracellular matrix	R_s	Solution resistance
EDS	Energy-dispersive X-ray spectroscopy	SBF	Simulated body fluid
EDTA	Ethylenediamine tetraacetic acid	SCE	Saturated calomel electrode
EIS	Electrochemical impedance spectroscopy	SEM	Scanning electron microscopy
FBS	Fetal bovine serum	SI	Squeeze casting infiltration
f-CNT	Functionalized carbon nanotube	SWCNT	Single-walled carbon nanotube
FESEM	Field emission scanning electron microscope	UV	Ultraviolet
FTIR	Fourier transform infrared	WCA	Water contact angle
HAp	Hydroxyapatite	WE	Working electrode
hADSC	Human adipose mesenchymal stem cell	XRD	X-ray diffraction
i_{corr}	Corrosion current density		

References

[1] Zhang, Y., et al., Influence of surface pre-treatment on the deposition and corrosion properties of hydrophobic coatings on a magnesium alloy. Corrosion Science, 2016. 112: 483-494.

[2] Lin, D.-J., et al., Tailored coating chemistry and interfacial properties for construction of bioactive ceramic coatings on magnesium biomaterial. Materials & Design, 2016. 89: 235-244.

[3] Jabbarzare, S., et al., Effect of graphene oxide on the corrosion, mechanical and biological properties of Mg-based nanocomposite. International Journal of Minerals, Metallurgy and Materials, 2022. 29(2): 305-319.

[4] Yang, Y., et al., Research advances of magnesium and magnesium alloys worldwide in 2022. Journal of Magnesium and Alloys, 2023. 11(8): 2611-2654.

[5] Huang, Y., et al., Development and prospects of degradable magnesium alloys for structural and functional applications in the fields of environment and energy. Journal of Magnesium and Alloys, 2023. 11(11): 3926-3947.

[6] Badkoobeh, F., et al., Additive manufacturing of biodegradable magnesium-based materials: Design strategies, properties, and biomedical applications. Journal of Magnesium and Alloys, 2023. 11(3): 801-839.

[7] Gu, X.N., et al., A study on alkaline heat treated Mg–Ca alloy for the control of the biocorrosion rate. Acta Biomaterialia, 2009. 5(7): 2790-2799.

[8] Rastegari, S. and E. Salahinejad, Surface modification of Ti-6Al-4V alloy for osseointegration by alkaline treatment and chitosan-matrix glass-reinforced nanocomposite coating. Carbohydrate Polymers, 2019. 205: 302-311.

[9] Mohemi, K., et al., Synthesis, Corrosion, and Bioactivity Evaluation of the Hybrid Anodized Polycaprolactone Fumarate/Silicon- and Magnesium-Codoped Fluorapatite Nanocomposite Coating on AZ31 Magnesium Alloy. Physical Mesomechanics, 2022. 25(1): 85-96.

[10] Zhang, L.-C., et al., Biofunctionization of biodegradable magnesium alloy to improve the in vitro corrosion resistance and biocompatibility. Applied Surface Science, 2018. 451: 20-31.

[11] Zhou, H., et al., Magnesium-based biomaterials as emerging agents for bone repair and regeneration: from mechanism to application. Journal of Magnesium and Alloys, 2021. 9(3): 779-804.

[12] Esmaili, S., et al., Corrosion Behavior and Biocompatibility of Graphene Oxide-Plasma Electrolytic Oxidation Coating on Magnesium Alloy. Physical Mesomechanics, 2022. 25(6): 583-599.

[13] Chen, J., et al., Synthesizing a multifunctional polymer to construct the catalytically NO-generating coating for improving corrosion resistance and biocompatibility of the magnesium alloy stent materials. Progress in Organic Coatings, 2024. 186: 108058.
[14] Wang, T., et al., A chitosan/polylactic acid composite coating enhancing the corrosion resistance of the bio-degradable magnesium alloy. Progress in Organic Coatings, 2023. 178: p. 107469.
[15] Zhao, Z., et al., Dual strengthened corrosion control of biodegradable coating on magnesium alloy for vascular stent application. Progress in Organic Coatings, 2023. 174: 107297.
[16] Panahi, P., et al., A review of the characterization methods for self-healing assessment in polymeric coatings. Progress in Organic Coatings, 2024. 186: 108055.
[17] Jiang, S., et al., Effect of alkali/acid pretreatment on the topography and corrosion resistance of as-deposited CaP coating on magnesium alloys. Journal of Alloys and Compounds, 2019. 793: 202-211.
[18] Bai, J., et al., Applications of magnesium alloys for aerospace: A review. Journal of Magnesium and Alloys, 2023. 11(10): 3609-3619.
[19] Li, K., et al., Selective laser melting of magnesium alloys: Necessity, formability, performance, optimization and applications. Journal of Materials Science & Technology, 2023. 154: 65-93.
[20] Dua, S., et al., Conjugated polymer-based composites for anti-corrosion applications. Progress in Organic Coatings, 2024. 188: 108231.
[21] Cheng, M., et al., Build a bridge from polymeric structure design to engineering application of self-healing coatings: A review. Progress in Organic Coatings, 2022. 167: 106790.
[22] Huangfu, H., et al., A smart composite coating with self-reporting and self-healing functions to enhance corrosion protection for magnesium alloys. Progress in Organic Coatings, 2023. 181: 107598.
[23] Peng, B., et al., Additive manufacturing of porous magnesium alloys for biodegradable orthopedic implants: Process, design, and modification. Journal of Materials Science & Technology, 2024. 182: 79-110.
[24] Li, X., et al., Corrosion resistance of dicalcium phosphate dihydrate/poly(lactic-co-glycolic acid) hybrid coating on AZ31 magnesium alloy. Corrosion Science, 2016. 102: 209-221.
[25] Jin, T., et al., Corrosion resistance of copolymerization of acrylamide and acrylic acid grafted graphene oxide composite coating on magnesium alloy. Progress in Organic Coatings, 2019. 136: 105222.
[26] Kumar, S.S.A., et al., New perspectives on Graphene/Graphene oxide based polymer nanocomposites for corrosion applications: The relevance of the Graphene/Polymer barrier coatings. Progress in Organic Coatings, 2021. 154: 106215.
[27] Li, L.-Y., et al., Advances in functionalized polymer coatings on biodegradable magnesium alloys – A review. Acta Biomaterialia, 2018. 79: 23-36.
[28] Pan, K., et al., Preparation of photo-crosslinked aliphatic polycarbonate coatings with predictable degradation behavior on magnesium-alloy stents by electrophoretic deposition. Chemical Engineering Journal, 2022. 427: 131596.
[29] Hatami, N., et al., Preparation of PCLF/Si–Mg–FA Nanocomposite Coating on Ti-based Alloy: Synthesis, Corrosion behavior and Cytocompatibility. Protection of Metals and Physical Chemistry of Surfaces, 2023. 59(2): 191-198.
[30] Song, C., et al., Electrochemical polymerization of dopamine with/without subsequent PLLA coating on Mg-Zn-Y-Nd alloy. Materials Letters, 2019. 252: 202-206.
[31] Liu, S., et al., Current applications of poly(lactic acid) composites in tissue engineering and drug delivery. Composites Part B: Engineering, 2020. 199: 108238.
[32] Daavari, M., et al., In vitro corrosion-assisted cracking of AZ31B Mg alloy with a hybrid PEO+MWCNTs/PCL coating. Surfaces and Interfaces, 2023. 42: 103446.
[33] Wang, Y., et al., Improved fracture toughness and ductility of PLA composites by incorporating a small amount of surface-modified helical carbon nanotubes. Composites Part B: Engineering, 2019. 162: 54-61.

[34] Bortoli, L.S.D., et al., Functionalized carbon nanotubes for 3D-printed PLA-nanocomposites: Effects on thermal and mechanical properties. Materials Today Communications, 2022. 31: 103402.
[35] Chong, W.J., et al., Additive manufacturing of antibacterial PLA-ZnO nanocomposites: Benefits, limitations and open challenges. Journal of Materials Science & Technology, 2022. 111: 120-151.
[36] Yaghoubi, A. and A. Ramazani, Anticancer DOX delivery system based on CNTs: Functionalization, targeting and novel technologies. Journal of Controlled Release, 2020. 327: 198-224.
[37] Xia, L., et al., Facile construction of Ag nanoparticles encapsulated into carbon nanotubes with robust antibacterial activity. Carbon, 2018. 130: 775-781.
[38] Herkendell, K., et al., Domination of volumetric toughening by silver nanoparticles over interfacial strengthening of carbon nanotubes in bactericidal hydroxyapatite biocomposite. Materials Science and Engineering: C, 2014. 34: 455-467.
[39] Chen, H., et al., Broad-Spectrum Antibacterial Activity of Carbon Nanotubes to Human Gut Bacteria. Small, 2013. 9(16): 2735-2746.
[40] Liu, S., et al., Sharper and Faster "Nano Darts" Kill More Bacteria: A Study of Antibacterial Activity of Individually Dispersed Pristine Single-Walled Carbon Nanotube. ACS Nano, 2009. 3(12): 3891-3902.
[41] Zhu, Y., et al., Growth and characterization of Mg(OH)2 film on magnesium alloy AZ31. Applied Surface Science, 2011. 257(14): 6129-6137.
[42] Kim, J.D., et al., Antibacterial activity and reusability of CNT-Ag and GO-Ag nanocomposites. Applied Surface Science, 2013. 283: 227-233.
[43] Munir, K.S., C. Wen, and Y. Li, Carbon Nanotubes and Graphene as Nanoreinforcements in Metallic Biomaterials: a Review. Advanced Biosystems, 2019. 3(3): 1800212.
[44] Arumugam, S. and Y. Ju, Carbon nanotubes reinforced with natural/synthetic polymers to mimic the extracellular matrices of bone – a review. Materials Today Chemistry, 2021. 20: 100420.
[45] Amiryaghoubi, N., et al., Recent advances in polymeric scaffolds containing carbon nanotube and graphene oxide for cartilage and bone regeneration. Materials Today Communications, 2021. 26: 102097.
[46] Cirillo, G., et al., Incorporation of carbon nanotubes into a gelatin–catechin conjugate: Innovative approach for the preparation of anticancer materials. International Journal of Pharmaceutics, 2013. 446(1): 176-182.
[47] Kang, S., M.S. Mauter, and M. Elimelech, Physicochemical Determinants of Multiwalled Carbon Nanotube Bacterial Cytotoxicity. Environmental Science & Technology, 2008. 42(19): 7528-7534.
[48] Abazari, S., et al., Functionalized carbon nanotube-encapsulated magnesium-based nanocomposites with outstanding mechanical and biological properties as load-bearing bone implants. Materials & Design, 2022. 213: 110354.
[49] Zhang, L., et al., Facile Preparation of Poly(lactic acid)/Brushite Bilayer Coating on Biodegradable Magnesium Alloys with Multiple Functionalities for Orthopedic Application. ACS Applied Materials & Interfaces, 2017. 9(11): 9437-9448.
[50] Bengoa, L.N., et al., Self-lubricating Cu-MWCNT coatings deposited from an ecofriendly glutamate-based electrolyte. Surface and Coatings Technology, 2020. 388: 125590.
[51] Shuai, C., et al., nMgO-incorporated PLLA bone scaffolds: Enhanced crystallinity and neutralized acidic products. Materials & Design, 2019. 174: 107801.
[52] Abazari, S., A. Shamsipur, and H.R. Bakhsheshi-Rad, Synergistic effect of hybrid reduced graphene oxide (rGO) and carbon nanotubes (CNTs) reinforcement on microstructure, mechanical and biological properties of magnesium-based composite. Materials Chemistry and Physics, 2023. 301: 127543.
[53] Abazari, S., et al. Carbon Nanotubes (CNTs)-Reinforced Magnesium-Based Matrix Composites: A Comprehensive Review. Materials, 2020. 13(19): 4421.

[54] Khazeni, D., M. Saremi, and R. Soltani, Development of HA-CNTs composite coating on AZ31 magnesium alloy by cathodic electrodeposition. Part 1: Microstructural and mechanical characterization. Ceramics International, 2019. 45(9): 11174-11185.
[55] Mizutani, Y., et al., Anodizing of Mg alloys in alkaline solutions. Surface and Coatings Technology, 2003. 169-170: 143-146.
[56] Li, L.-H., et al., Deposition of microarc oxidation–polycaprolactone duplex coating to improve the corrosion resistance of magnesium for biodegradable implants. Thin Solid Films, 2014. 562: 561-567.
[57] Kondoh, K., et al., Characteristics of powder metallurgy pure titanium matrix composite reinforced with multi-wall carbon nanotubes. Composites Science and Technology, 2009. 69(7): 1077-1081.
[58] Zhu, J., et al., In situ stabilized carbon nanofiber (CNF) reinforced epoxy nanocomposites. Journal of Materials Chemistry, 2010. 20(23): 4937-4948.
[59] Lim, D.G., et al., Combinatorial nanodiamond in pharmaceutical and biomedical applications. International Journal of Pharmaceutics, 2016. 514(1): 41-51.
[60] Partha, R. and J.L. Conyers, Biomedical applications of functionalized fullerene-based nanomaterials. International Journal of Nanomedicine, 2009. 4: 261-275.
[61] Montellano, A., et al., Fullerene C60 as a multifunctional system for drug and gene delivery. Nanoscale, 2011. 3(10): 4035-4041.
[62] Musameh, M., et al., Low-potential stable NADH detection at carbon-nanotube-modified glassy carbon electrodes. Electrochemistry Communications, 2002. 4(10): 743-746.
[63] Bonfield, W., Designing Porous Scaffolds for Tissue Engineering. Philosophical Transactions: Mathematical, Physical and Engineering Sciences, 2006. 364(1838): p. 227-232.
[64] Wang, G., et al., A co-dispersion nanosystem of graphene oxide @silicon-doped hydroxyapatite to improve scaffold properties. Materials & Design, 2021. 199: 109399.
[65] Pantarotto, D., et al., Translocation of bioactive peptides across cell membranes by carbon nanotubes. Chemical Communications, 2004(1): 16-17.
[66] Ding, N., X. Chen, and C.-M.L. Wu, Mechanical properties and failure behaviors of the interface of hybrid graphene/hexagonal boron nitride sheets. Scientific Reports, 2016. 6(1): 31499.
[67] Wu, W., et al., Biocorrosion resistance and biocompatibility of Mg–Al layered double hydroxide/poly-L-glutamic acid hybrid coating on magnesium alloy AZ31. Progress in Organic Coatings, 2020. 147: 105746.
[68] Hussein MA, Azeem MA, Kumar AM, Emara NM. Processing and in vitro corrosion analysis of sustainable and economical eggshell reinforced Mg and Mg-Zr matrix composite for biomedical applications. Materials Today Communications. 2022;32:103944.
[69] Kujur MS, Manakari V, Parande G, Prasadh S, Wong R, Mallick A, Gupta M. Effect of samarium oxide nanoparticles on degradation and invitro biocompatibility of magnesium. Materials Today Communications. 2021;26:102171.
[70] Lavanya K, Abinaya S, Selvamurugan N. Recent advances in one-dimensional nanowire-incorporated bone tissue engineering scaffolds. Materials Today Communications. 2022; 33: 104229.
[71] Amiryaghoubi N, Fathi M, Barzegari A, Barar J, Omidian H, Omidi Y. Recent advances in polymeric scaffolds containing carbon nanotube and graphene oxide for cartilage and bone regeneration. Materials Today Communications. 2021;26:102097.
[72] Francis AP, Augustus AR, Chandramohan S, Bhat SA, Priya VV, Rajagopalan R. A review on biomaterials-based scaffold: An emerging tool for bone tissue engineering. Materials Today Communications. 2023;34:105124.
[73] Hussain M, Khan SM, Al-Khaled K, Ayadi M, Abbas N, Chammam W. Performance analysis of biodegradable materials for orthopedic applications. Materials Today Communications. 2022;31:103167.

Declaration of interests

☒ The authors declare that they have no known competing financial interests or personal relationships that could have appeared to influence the work reported in this paper.

Author Statement

All persons who meet authorship criteria are listed as authors, and all authors certify that they have participated sufficiently in the work to take public responsibility for the content, including participation in the concept, design, analysis, writing, or revision of the manuscript. Furthermore, each author certifies that this material or similar material has not been and will not be submitted to or published in any other publication before its appearance in the Materials Today Communications.

Author Contributions: Methodology, formal analysis, writing—original draft preparation, **H. Abrari-Bahirlooei, M.T. Dehaghani, M. Amiri, M. Razzaghi**; Conceptualization, supervision, writing—review and editing, **T. Ahmadi, V. Nekouie, H.R. Bakhsheshi-Rad**. All authors have read and agreed to the published version of the manuscript.